



Facile Hydrothermal Synthesis of Hollow Fe_3O_4 Nanospheres: Effect of Hydrolyzing Agents and Electrolytes on Electrocapacitive Performance of Advanced Electrodes

SR Mishra^{1*}, H Adhikari¹, DL Kunwar¹, C Ranaweera², B Sapkota³, Madhav Ghimire¹, R Gupta² and J Alam¹

¹Department of Physics and Materials Science, The University of Memphis, USA

²Department of Chemistry, Pittsburg State University, USA

³Department of Physics, Northeastern University, USA

Abstract

In this work, the effect of hydrolyzing agents such as urea, Ammonium Bicarbonate (ABC), Dodecylamine (DDA) on morphology, size and electrochemical activity of Fe_3O_4 nanospheres was investigated. For comparison, Fe_3O_4 nanospheres were also synthesized without a hydrolyzing agent. The structural and morphological assessment of the synthesized Fe_3O_4 nanopowder was performed using x-ray diffraction, scanning electron microscopy and surface area analysis. The room temperature magnetic properties were studied via vibrating sample magnetometer. The scanning electron microscopy images showed nanospheres of Fe_3O_4 with a range of sizes (150–330 nm) which depend on hydrolyzing agents used. All the synthesized samples were crystalline in structure with a distinct signature of magnetite phase. The surface area analysis indicated that these particles were mesoporous in nature. Electrochemical characteristics were investigated using cyclic voltammetry and galvanostatic measurements. Cyclic voltammetry measurements were performed in three different electrolytes viz. KOH, NaOH, and LiOH and observed that specific capacitance of the synthesized Fe_3O_4 depends on the electrolyte used. The relatively high specific capacitance of 173.8 F/g was observed for Fe_3O_4 prepared using DDA in 3M KOH electrolyte. Fe_3O_4 -DDA also showed excellent cyclic stability as well, retaining 107% of specific capacitance value at up to 5,000 cycles measured. The study clearly elucidates the effect of the hydrolyzing agent on physical and morphological properties of Fe_3O_4 . In addition, through electrochemical testing, the study illustrates the choice of aqueous electrolyte in optimizing the electrocapacitive performance of Fe_3O_4 nanospheres.

Keywords

Fe_3O_4 nanospheres, Electrochemical, Cyclic voltammetry, Specific capacitance

Introduction

Among various electrical energy storage devices, electrochemical capacitors, aka super capacitors, are unique in terms of high power density, high charge-discharge cycle life, and wide temperature range operation [1]. When the charges are stored on the surface of the electrodes

in these capacitors, then these capacitors are known as Electrical Double Layer Capacitors (EDLC). Along with surface charges, if the charge transfer takes place between the electrode and the electrolyte then these capacitors are termed as pseudocapacitors [2]. Usually, carbon based materials fall into the first category of EDLC where

***Corresponding author:** SR Mishra, Department of Physics and Materials Science, The University of Memphis, Memphis, TN 38152, USA, E-mail: srmishra@memphis.edu

Received: June 19, 2017: **Accepted:** September 02, 2017: **Published:** September 04, 2017

Copyright: © 2017 Mishra SR, et al. This is an open-access article distributed under the terms of the Creative Commons Attribution License, which permits unrestricted use, distribution, and reproduction in any medium, provided the original author and source are credited.

Citation: Mishra SR, Adhikari H, Kunwar DL, Ranaweera C, Sapkota B, et al. (2017) Facile Hydrothermal Synthesis of Hollow Fe_3O_4 Nanospheres: Effect of Hydrolyzing Agents and Electrolytes on Electrocapacitive Performance of Advanced Electrodes. Int J Metall Met Phys 2:007

no charge transfer takes place (non-Faradic), while many oxides such as RuO_2 , MnO_2 , Co_3O_4 , and NiCo_2O_4 fall under the category of pseudocapacitors where redox reaction takes place between the electrode and the electrolyte (Faradic) [3]. Furthermore, pseudocapacitor metal-oxide electrodes are considered, as suitable cathode materials as it possesses multiple accessible valence states [4,5]. However, these materials are severely restricted when served as the positive electrode materials due to the low hydrogen evolution potential in aqueous solution. Owning higher hydrogen evolution potential in aqueous solution in comparison to other metal oxides (e.g. MnO_2 or NiO), iron oxide can serve as promising anode material in asymmetrical electro capacitors [6]. Besides, iron oxide is attractive materials because of natural abundance, low cost, and being environmental friendly material [7].

Among ternary oxides, such as NiCo_2O_4 , Mn_2O_3 , Co_3O_4 , Fe_3O_4 , and some composites have been identified as the potential electrode materials in view of the low-cost and environmentally friendly material as pseudocapacitor [8-14]. Considering the fact that pseudocapacitive behavior of nanostructured oxide depends largely on their surface area, pore volume density, and electrical conductivity various attempts have been made to optimize these parameters to gain high electrochemical activity from these materials. Besides morphological parameters, the type of electrolytes and their molar concentration play an important role in determining the electrochemical behavior of oxide electrodes [14-16]. Therefore, many aqueous electrolytes such as H_2SO_4 , KOH, K_2SO_4 , KCl, KNO_3 , NaOH, Na_2SO_4 , NaCl, LiOH, Li_2SO_4 etc. have been explored as electrolytes in supercapacitors [17-21]. Large capacitances in Fe_3O_4 have been reported in alkali sulfites and sulfate solutions [14,22-25]. In fact, the choice of ideal electrolyte depends on the electrode material properties and intercalation efficiency of the cations, which ultimately lead to the resulting performance of supercapacitor devices [26].

Considering the influence of above two factors, viz. morphology and electrolyte, on pseudocapacitive behavior oxide electrodes, an attempt is made herein to understand the influence of these two factors with Fe_3O_4 being a model electrode system. The study focuses on hollow mesoporous Fe_3O_4 nanosphere as this morphology may offer a high surface area with increased electroactive sites. In this study, facile one-step and template free solvothermal approach was adapted to obtain Fe_3O_4 nanospheres, using Ethylene Glycol (EG) as a reaction solvent and utilizing different hydrolyzing sources such as urea, ABC and DDA and their electrocapacitive behavior was assessed in three different electrolytes viz. KOH, NaOH, and LiOH. The presented synthesis method for hollow Fe_3O_4 is comparatively better than the one using surfac-

tants or amines, in terms of cost and hazard [27-30]. The results were compared with Fe_3O_4 nanospheres prepared without any hydrolyzing agent. Specific capacitance as high as 173.8 F/g at 5 mV/s scan rate and power density approaching 1200 W/g was observed for some Fe_3O_4 samples. In fact, higher electrocapacitive performance was observed for electrodes assessed with KOH electrolyte.

Experiment

Template free synthesis of Fe_3O_4 hollow spheres

Ferric Chloride Hexahydrate ($\text{FeCl}_3 \cdot 6\text{H}_2\text{O}$), Urea ($\text{H}_2\text{N}-\text{CO}-\text{NH}_2$), Ethylene Glycol (EG), Sodium Acetate (NaAc), Ethanol ($\text{C}_2\text{H}_5\text{OH}$), Ammonium Bicarbonate (NH_4HCO_3 , ABC), Dodecylamine ($\text{CH}_3(\text{CH}_2)_{10}\text{CH}_2\text{NH}_2$, DDA) were purchased from Sigma Aldrich. All the chemicals and solvents were of analytical grade and used without further purification. In the experimental process, the inorganic $\text{FeCl}_3 \cdot 6\text{H}_2\text{O}$ was used as a source of iron and EG as a mild reducing agent during the reaction process. Urea, ABC, and DDA were used to guide the formation of the hollow magnetite spheres, and to control their size distribution.

In a typical experiment, 6 mmol of $\text{FeCl}_3 \cdot 6\text{H}_2\text{O}$ and 0.06 mol of urea (or 12 mmol ABC or 6 mmol of DDA) were dissolved in 35 mL of EG under magnetic stirring to form a clear solution. Then, the mixture was transferred to a 50 mL Teflon-lined autoclave and maintained at 200 °C for 12 h [31]. After the autoclave was cooled to ambient temperature, the products were obtained by centrifuging and washing with distilled water and absolute ethyl alcohol several times, followed by drying in a vacuum oven at 60 °C for 8 h. The inorganic salt $\text{FeCl}_3 \cdot 6\text{H}_2\text{O}$ was used as an iron source. EG as a mild reducing agent, and urea, ABC and DDA were used to as ammonia source ($(\text{NH})_4$ -Source) to guide the formation of the hollow magnetite spheres. As prepared samples in the presence of urea, ABC and DDA are labeled as Fe_3O_4 -urea and Fe_3O_4 -ABC, and Fe_3O_4 -DDA, respectively.

Synthesis of Fe_3O_4 hollow spheres using carbon template

Mixtures of 40 mg of glucose derived carbon nanospheres via hydrothermal method [32], 30 ml of Ethylene Glycol (EG), 1.35 gm of $\text{FeCl}_3 \cdot 6\text{H}_2\text{O}$, 2.46 gm of NaAc were mixed using ultrasonication for 30 min. The solution was then transferred to 45 ml Teflon-line autoclave and heated at 180 °C for 12 hrs. The autoclave was cooled down to room temperature and the precipitate was washed with DI water and ethanol for several times. Finally, it was dried at 70 °C in a vacuum oven for 8 h. Later the samples were heated at 350 °C for 5 h. to remove carbon template. The Fe_3O_4 nanospheres via carbon template are labeled as Fe_3O_4 -CNS.

The X-Ray Diffraction (XRD) patterns were collected using Bruker D8 Advance X-ray diffractometer using Cu K α radiation ($\lambda \sim 0.154056$ nm). Scanning Electron Microscopy (Philips XL 30 environmental scanning electron microscope, SEM) operated at 3 keV was employed to analyze the morphology of the samples. The surface area and pore volume analysis were performed using N2 adsorption-desorption isotherms using carried out using Autosorb-1, (Quantachrome, Boynton Beach, FL 33426, model No. AS1MP) using nitrogen as adsorbing gas at 77 K. The magnetic properties of the samples were investigated at room temperature using Vibrating Sample Magnetometer (VSM).

Electrochemical measurements were performed using the standard three-electrode system on a Versastat 4-500 electrochemical workstation (Princeton Applied Research, USA). The working electrode was prepared by mixing 80 wt.% of the synthesized sample, 10 wt.% of acetylene black and 10 wt.% of Polyvinylidene Difluoride (PVDF) in the presence of N-Methyl Pyrrolidinone (NMP). After mixing the components, the slurry was pasted onto nickel foam. The prepared electrode was dried at 60 °C under vacuum for 10 hrs. The loading mass of all samples on nickel foam was about 2-3 mg. The deposited weight was accurately measured by weighing the nickel foam before and after deposition with an analytical balance (model MS105DU, Mettler Toledo, max. 120 g, 0.01 mg of resolution). A platinum wire as a counter electrode, Saturated Calomel Electrode (SCE) as a reference electrode, and synthesized samples on nickel foam as a working electrode were used. The electrochemical performance of the electrodes was evaluated by Cyclic Voltammetry (CV) and galvanostatic charge-discharge techniques in three different electrolytes viz. 3M KOH, NaOH, and LiOH.

Results and Discussion

The phase of the prepared- Fe_3O_4 was determined by using powder X-Ray Diffraction (XRD) spectroscopy, Figure 1. The diffraction peaks for all samples could be indexed to the magnetite syn - Fe_3O_4 phase having a cubic spinel structure (ICDD Card No. 76-5948). The peaks indexed as planes (220), (311), (400), (422), (511) and (440) corresponded to a cubic unit cell, characteristic of a cubic spinel structure [33]. The absence of other peaks reflects that high-purity Fe_3O_4 hollow nanospheres were synthesized. Also, the diffraction peaks are narrower for samples prepared using hydrolyzing agents where as Fe_3O_4 -CNS show broad diffraction peaks, indicating the presence of finer crystallites in later samples. The peaks of (220), (311), (400), (422), (511) and (440) have been deconvoluted to Lorentzian curves, using Peak Fit software for the determination of FWHM value of the

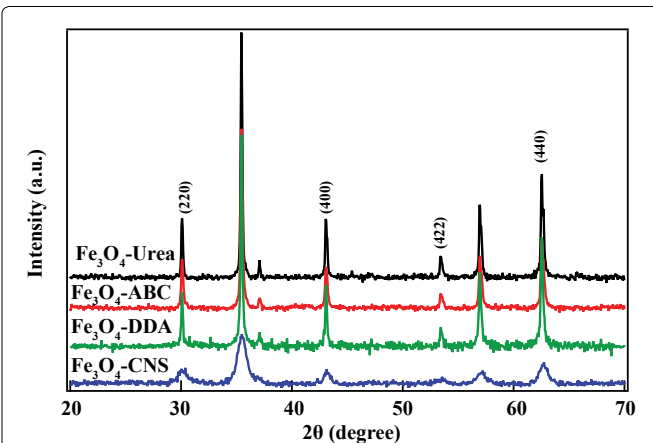


Figure 1: XRD pattern of Fe_3O_4 prepared with different hydrolyzing agents.

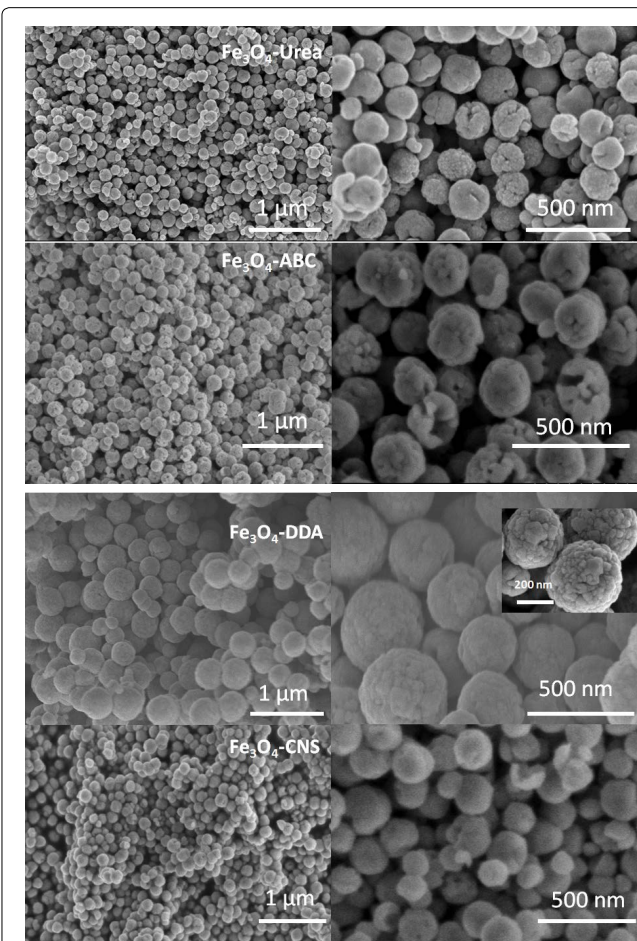


Figure 2: FE-SEM images of Fe_3O_4 nanospheres prepared using different hydrolyzing agents.

indexed peaks [34]. The crystallite size of Fe_3O_4 was obtained using Scherrer's formula [35] using the FWHM value of the respective indexed peaks. The average crystallite size was 48, 40, 56, and 8 nm for Fe_3O_4 -urea, Fe_3O_4 -ABC, Fe_3O_4 -DDA, and Fe_3O_4 -CNS samples, respectively. Higher crystallinity displayed by Fe_3O_4 -DDA sample indicate better ionic bonding of ions in Fe_3O_4 .

The morphology of samples was investigated by Field Emission Scanning Electron Microscope (FE-SEM). Figure 2 shows the representative SEM images of as-obtained Fe_3O_4 synthesized using different hydrolyzing agents. It is observed that the samples were monodispersed nanostructured hollow spheres without any agglomeration. The rough surface of the spheres implies that the surface of the hollow spheres is composed of closely packed nanoparticles. Figure 3 shows SEM based diameter distribution of Fe_3O_4 nanospheres as prepared using different hydrolyzing agents. The average diameter for Fe_3O_4 -urea, Fe_3O_4 -ABC, Fe_3O_4 -DDA, and Fe_3O_4 -CNS samples was observed to be ~ 172 , 206 , 322 , 157 nm, respectively. Overall, smallest size Fe_3O_4 were obtained without the use of any hydrolyzing agent.

Schematic illustration of the formation mechanism of hollow assembly of iron-hydroxyl ions is shown in Figure 4. Under the hydrothermal condition, the ammonia source ($(\text{NH}_4)_4$ -sources) gradually decomposed into NH_3 and CO_2 [36]. Further NH_3 reacts with water to produce

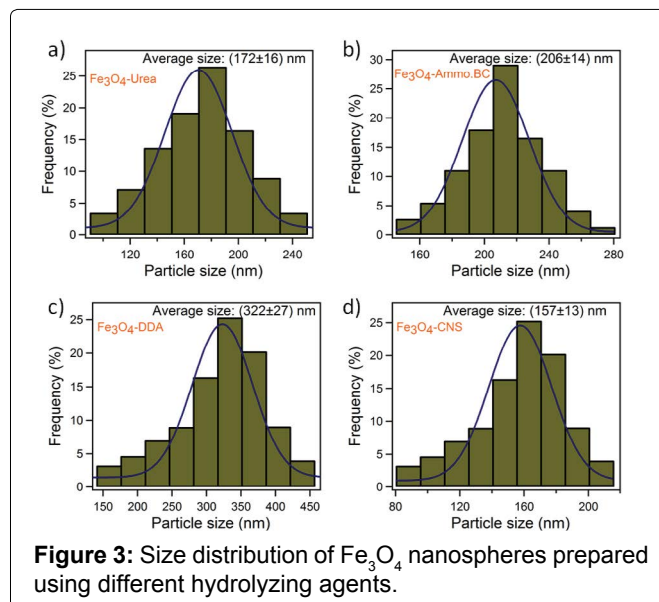


Figure 3: Size distribution of Fe_3O_4 nanospheres prepared using different hydrolyzing agents.

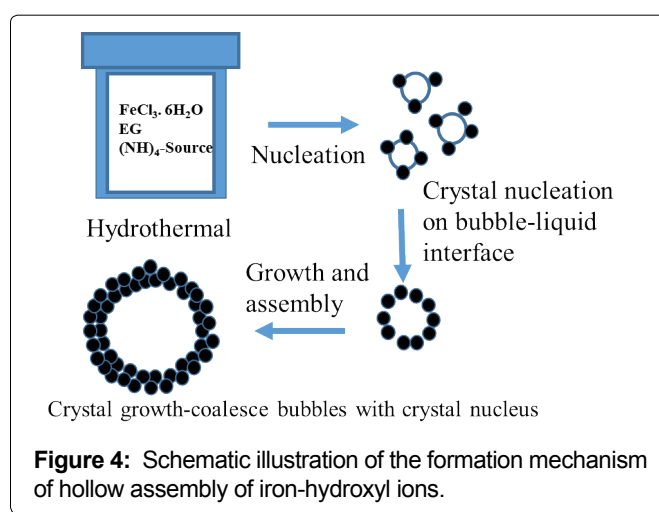
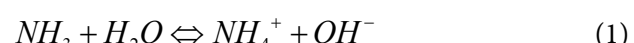
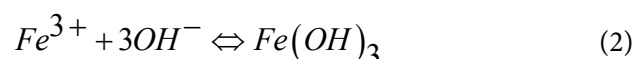


Figure 4: Schematic illustration of the formation mechanism of hollow assembly of iron-hydroxyl ions.

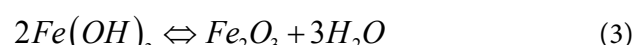
NH_4^+ and OH^- . In the oxide crystal growth process, tiny crystalline nuclei are formed, and nanoparticles of this oxide get precipitated by an increase in pH due to NH_4^+ ions generated from NH_3 as a result of decomposition of ammonia-source with increased temperature. The hydrolysis of ammonia-source leads to a rise in the pH due to increased release of NH_4^+ in the solution. The hydrolysis progresses slowly, and the basic solution undergoes supersaturation of the metal-hydroxide species [37,38]. At the same time, gaseous bubbles of ammonia and carbon dioxide having high surface energy may provide the heterogeneous nucleation site for newly formed nanocrystallites to aggregate around the surface of the bubbles. The spherical shape is then formed by aggregation of the original crystals of iron-hydroxyl nucleated on the liquid-bubbles interface to minimize the surface energy, and then an original inner core was formed. Thus, the formation of metal-hydroxide crystal assembly into spherical order. It is worth mentioning the fact that the crystal growth process proceeds with the delicate balance of crystal nucleus formation and the growth rate of the nucleus. If the formation speed of the crystal nucleus is faster than the growth rate of the nucleus, it will tend to form smaller size products and vice versa. In addition, crystal growth process is assisted by gas bubbles, which serve as seeds to assist the Ostwald ripening process. According to the formation of crystals, the rate of the generation or the quantity of the gas bubbles play a key role in modifying the particle sizes. At the higher rate of bubble production at the same time during nucleus formation, the quantity of oxide crystal aggregation in each bubble will be reduced, and the sizes of the obtained spheres will be decreased and vice versa. In fact, the rate of hydrolysis and ammonia content can be tuned to obtain oxide hollow spheres of different sizes. Spherical Fe_3O_4 nanospheres are formed upon oxidation at high temperature. The reaction leading to magnetite formation in presence of hydrolyzing agent rich in ammonia can be summarized as follow. Ammonium salts can be hydrolyzed in presence of trace amount of water coming out of $\text{FeCl}_3 \cdot 6\text{H}_2\text{O}$, resulting in NH_3 , H_2O , and CO_2 as a byproduct. NH_3 further reacts with water to form hydroxide anions as follow,



The use of Fe(III) salt leads to precipitation of hydroxide as follow:



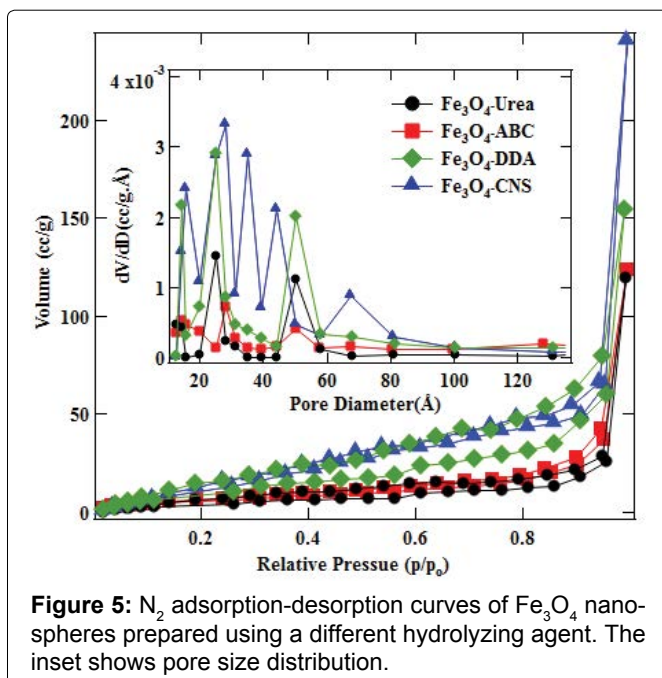
This leads to the formation of Fe_2O_3 as follow:



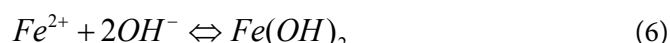
A mild reducing agent ethylene glycol was used in re-

Table 1: Physical and magnetic properties of as synthesized Fe_3O_4 nanospheres prepared with different hydrolyzing agents.

	Mean particle size (nm)	Crystallite size (nm)	BET surface area (m^2/g)	Magnetization (emu/g)	Coercivity (Oe)
Fe_3O_4 -urea	172 ± 16	33.99	17.08	82.89	160
Fe_3O_4 -ABC	206 ± 14	35.50	23.08	85.04	150
Fe_3O_4 -DDA	322 ± 27	36.33	53.04	84.67	154
Fe_3O_4 -CNS	157 ± 13	24.85	67.59	60.55	64

**Figure 5:** N_2 adsorption-desorption curves of Fe_3O_4 nanospheres prepared using a different hydrolyzing agent. The inset shows pore size distribution.

action to reduce Fe(III) to Fe(II) thus leading to the formation of Fe_3O_4 as follow. EG can undergo dehydration and the so-formed acetaldehyde, which reduces Fe(III) to Fe(II) [39-41],



Usually iron exist in both ferrous and ferric oxidation state leading to the formation of magnetite when subjected to high temperature,



The BET specific surface areas of the Fe_3O_4 was determined by N_2 adsorption-desorption isotherm curves measured at 77K between relative pressure $p/p_0 \sim 0.029$ to 0.99. All samples display a type IV isotherm with adsorption-desorption hysteresis, indicating the presence of mesopores in the sample [42], Figure 5. The measured BET surface area of Fe_3O_4 -urea, Fe_3O_4 -ABC, Fe_3O_4 -DDA and Fe_3O_4 -CNS samples are ~17, 23, 53, 67 m^2/g and are listed in Table 1. Figure 5 inset show pore size distribution obtained from BJH analysis. From the curve, it can be observed that the largest number of pores is distribut-

ed at around 2-6 nm for all Fe_3O_4 samples. These pores are attributed to the interparticle spaces. The narrow adsorption-desorption hysteresis loops are indicative of the presence of independent mesopores in Fe_3O_4 . The Fe_3O_4 -CNS samples show much higher surface area (67 m^2/g) and pore volume density. This indicates the fact that Fe_3O_4 -CNS might have relatively large number of pores as compared to samples prepared using hydrolyzing agents. The observed surface area of Fe_3O_4 samples is in fact much larger than the value of hollow spheres reported previously [43]. It is important to understand that the electrochemical super capacitance does heavily depend on the specific surface area of the electrode materials but as not all the specific surface area is electrochemically accessible when the material is in contact with an electrolyte, thus measured the capacitance of various materials does not linearly depend on the specific surface area. In fact, it largely depends upon the electrochemically useful area called electroactive surface area. The pore size of the electrode material also plays an important role in the electrochemical active surface area. According to Largeot, et al. [44] the pore size of electrode materials that yield maximum double-layer capacitance was very close to the electrolyte ion size (with respect to an ionic liquid electrolyte), and both larger and smaller pores led to a significant drop in capacitance. Considering the diameters of solvated ions ~3 nm [26,45], the best electrode materials for electrical double layer capacitor are those which use mesoporous electrode materials with open pores of 2.0-6.0 nm [44-47]. It is expected that the large BET surface area, as displayed by porous Fe_3O_4 nanospheres, can provide plenty of superficial electrochemical active sites to participate in the Faradaic redox reactions. Furthermore, appropriate pore size distribution, between 2-6 nm as observed for all Fe_3O_4 samples, Figure 5, can offer additional efficient transport pathway for electrolyte molecules to their interior voids during the charge/discharge storage process and give rise to the excellent electrochemical property of the electrode material, which is critical for the electrochemical performance [26].

The magnetic properties of Fe_3O_4 nanospheres were investigated by Measuring Magnetization vs. Applied Field (M vs. H) using Vibrating Sample Magnetometer (VSM) at room temperature in the field up to 1.2 T. The

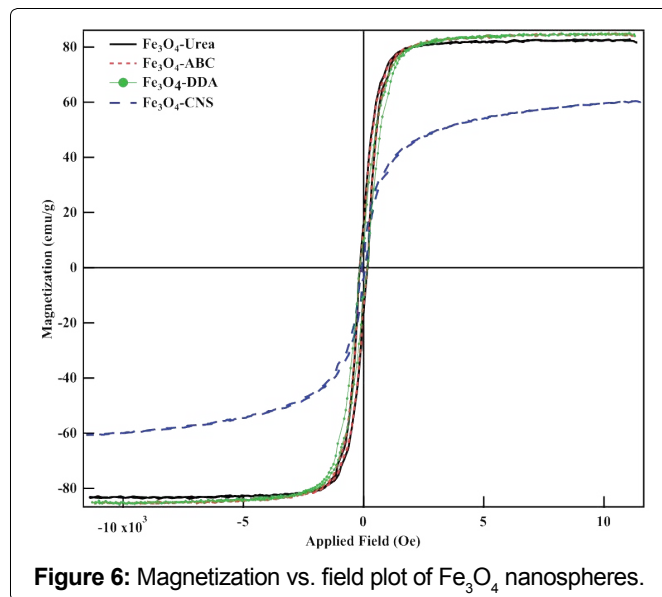


Figure 6: Magnetization vs. field plot of Fe_3O_4 nanospheres.

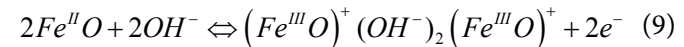
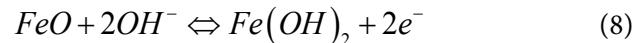
M vs. H plots are shown in Figure 6. The magnetic parameters extracted from M vs. H plots are listed in Table 1. Except for Fe_3O_4 -CNS all the hysteresis loops are well saturated within the field sweeping from -1.2 to 1.2 T. It is evident that the crystalline Fe_3O_4 prepared with the hydrolyzing agents show marked Saturation Magnetization (Ms) value of ~80 emu/g and display ferromagnetic behavior. The saturation magnetization values, Ms, for Fe_3O_4 -urea, Fe_3O_4 -ABC, Fe_3O_4 -DDA, and Fe_3O_4 -CNS samples are 82.8, 85.0, 84.6, and 60.5 emu/g, respectively. These measured Ms values are lower than the Ms value of the bulk Fe_3O_4 (Ms ~92 emu/g) [48,49]. However, these Ms values are much higher than the values reported for hollow structured magnetite [48,50]. The relative low observed Ms value of Fe_3O_4 hollow spheres as compared bulk could be due to canted spins, magnetically dead layer on the surface of the Fe_3O_4 nanospheres and could also be attributed to anisotropy, including crystal anisotropy and shape anisotropy [51]. The Fe_3O_4 -CNS display low Ms of ~60.5 emu/g with a component of super paramagnetic behavior. The small crystallite size of Fe_3O_4 -CNS sample may fall under the super paramagnetic limit, thus its magnetization does not saturation even in the high field range of 1.2 T value. All samples display significant coercivity. The coercivity value of Fe_3O_4 -urea, Fe_3O_4 -BC, Fe_3O_4 -DDA, and Fe_3O_4 -CNS is 160, 150, 154 and 64 Oe, respectively. It is not easy to point out single contribution to the coercivity in nanoparticles. The much-accepted rule of increase in coercivity with a decrease in particle size may not apply here, as several contributions to the coercivity such as size, oxygen vacancies, surface coordination, anisotropy constant determine the net coercivity of the material [52,53]. However, it can be argued that the spheres are made of nanosized Fe_3O_4 crystallites, thus higher values of HC could be attributed to the oriented assembly of particles into hollow spheres. This oriented

Table 2: Specific capacitances of Fe_3O_4 nanospheres evaluated in different electrolytes at a fixed scan rate of 5 mV/s.

	Specific capacitance (F/g) @ 5 mV/s scan rate		
	KOH	NaOH	LiOH
Fe_3O_4 -urea	173.5	113.8	90.84
Fe_3O_4 -ABC	164.1	112.7	94.95
Fe_3O_4 -DDA	173.8	160.7	162.7
Fe_3O_4 -CNS	190.1	110.7	107.6

assembly changes the single domain configuration of nanoparticles into multi-domain [54]. The observed low coercivity of Fe_3O_4 -CNS is again attributed to the presence of superparamagnetic nanocrystallites [55].

Cyclic Voltammetry (CV) and charge-discharge curves were measured to investigate the electrochemical behavior of Fe_3O_4 nanoparticles. Figure 7 show CV curves of Fe_3O_4 measured in three different electrolytes, viz. KOH, NaOH, and LiOH. The CV curves were measured in the voltage window of 0.0 to 0.6 V and were obtained at different scan rate from 5 to 200 mV/s. All the CV plots exhibit a pair of redox peaks associated with the redox reactions involved in the alkaline electrolyte during the charging and discharging process. A pair of redox peaks associated with the reversible reaction between Fe^{2+} and Fe^{3+} [56-58] is as follow,



The specific capacitance was calculated from the CV plot using the following equation [59].

$$C_{sp} = \frac{\int_{V_1}^{V_2} i \times V \times dv}{m \times v \times (V_2 - V_1)} \quad (10)$$

Where V_1 and V_2 are the limits of the working potential, i is the corresponding current, m is the mass of the electroactive materials, and v is the scan rate in mV/s. It is clear from the CV curves that the current response shows a proportional increase with the scan rate, indicating the good capacitive behavior of the electrode materials, which in turn can be ascribed to facile ion diffusion and large specific surface area of the electrode materials. Moreover, the shape of the CV curves is nearly independent of the scan rates, which can be attributed to the improved mass transportation and electron conduction of the electrode material [60]. Table 2 lists the specific capacitance of electrodes as obtained in the different electrolyte solution at 5 mV/s scan rate. Figure 5 compares specific capacitance as a function of scan rate of electrodes measured in different electrolytes. Highest specific capacitance was obtained for all samples measured in KOH electrolyte. For example, the specific ca-

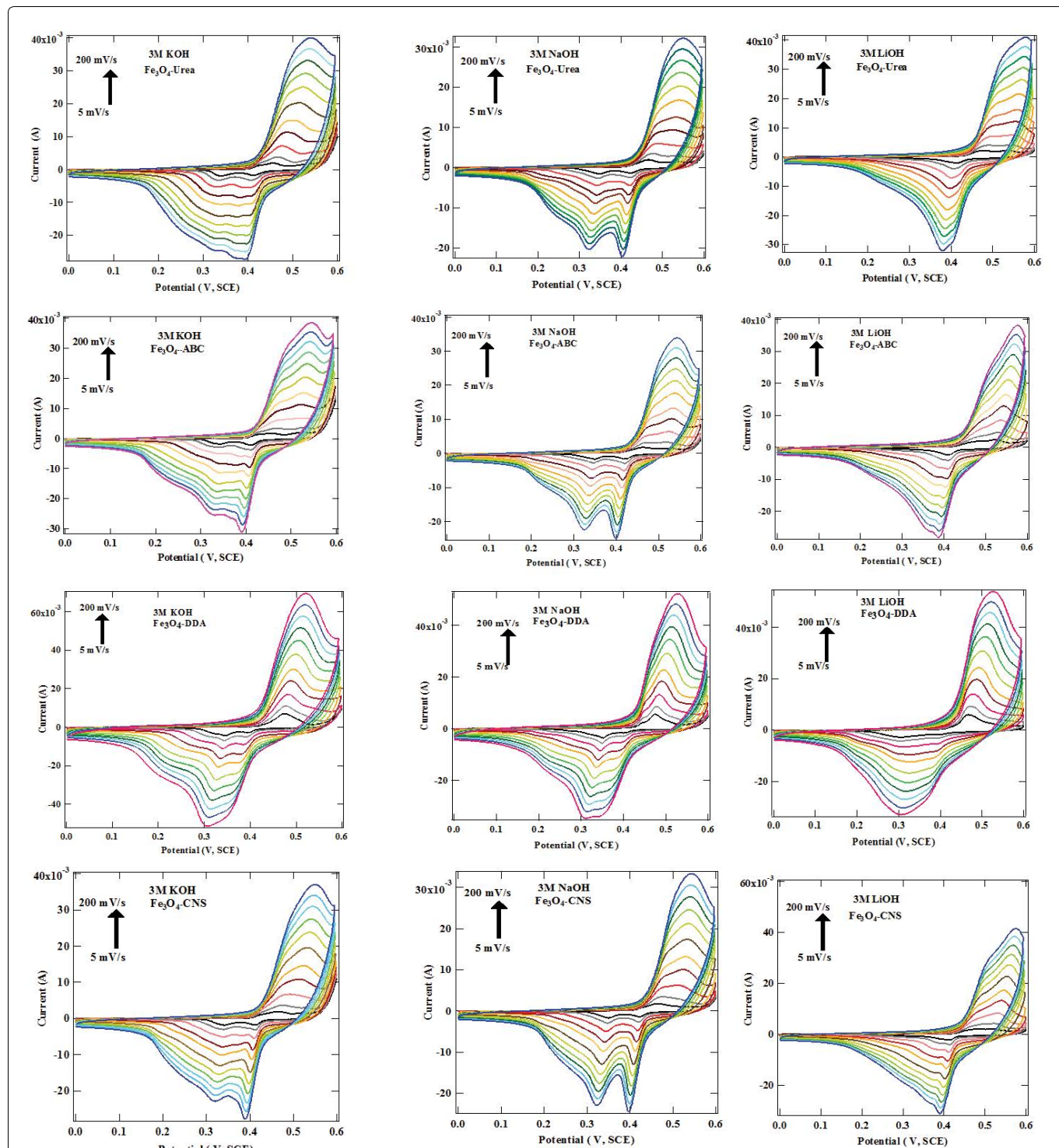


Figure 7: CV curves of Fe₃O₄ nanospheres measured in different electrolytes in a potential window of 0.0–0.6 V at different scanning rate from 5 mV/s to 300 mV/s.

pacitance measured for Fe₃O₄-urea, Fe₃O₄-ABC, Fe₃O₄-DDA, and Fe₃O₄-CNS in 3M KOH, at a low scan rate of 5 mV/s are, 173.5, 164.1, 173.8 and 190.1 F/g, respectively. However, among all samples, Fe₃O₄-DDA displayed relatively higher specific capacitance for all electrolytes and higher scan rates, Figure 8. This could be attributed to optimal electroactive surface and pore size distribution in Fe₃O₄-DDA as discussed below. Overall, the

specific capacitance was observed to decrease with the increase in scan rate. Previous results on Fe₃O₄ electrode prepared via sol-gel technique and studied under similar experimental conditions showed C_{sp} of ~185 F/g [61], hydrothermally prepared Fe₃O₄ thin film displayed C_{sp}~118.2 F/g [62], while Fe₃O₄-carbon nanotube composite showed C_{sp} of ~117.2 F/g [63]. In line with these observations, the Fe₃O₄ electrodes studied herein show

high specific capacitance of ~170-190 F/g at 5 mV/s in 3M KOH solution.

To study the effect of the hydrolyzing agent on their electroactive surface areas, CV data of Fe_3O_4 oxide electrodes has been analyzed by using the Randles-Sevcik mechanism: $i = (2.69 \times 105) n^{3/2} A D^{1/2} C_0 v^{1/2}$ [64,65]. Here, i represents the peak current (in Amp), n is ascribed to the electron number transferred during the charge/discharge process, A is attributed to the electroactive surface area (cm^2), D is the diffusion coefficient (cm^2/s), C_0 is the electrolyte concentration (mol/cm^3), and v is the scan rate (V/s) [66]. The electroactive surface area, i.e., the area that effectively transfers the charge to the species in solution. It depends on how well the electrolyte accesses the pores and is also influenced by the magnitude of the diffusion or Nernst layer in the electrolyte and the surface roughness, surface defects, and surface species of the electrode. It has a complex function of total surface area, pore size distribution, electrolytes used and temperature. Due to the similar redox reaction in the in a particular electrolyte solution for these electrodes, the diffusion coefficient, electrolyte concentration, and the scan rate are the same. Accordingly, i is mainly determined by the electron transfer number ($n^{3/2}$) and the electroactive

Surface Area (A), which are the two dominant roles to improve capacitance performance of supercapacitors. The peak currents for the anodic and cathodic processes can be obtained from the CV curves from Figure 7. By plotting these peak current magnitudes vs. square roots of the scan rate (V/s), Figure 9, a linear fit with the surface area of the electrode equal to the slope (S)/($2.69 \times 10^5 n^{3/2} D^{1/2} C_0$) was obtained. For 3M KOH concentrated solution, with $n=1$, and $D=1.957 \times 10^{-5} \text{ cm}^2/\text{s}$ [66,67], the electroactive area A can be derived as $A = (\text{slope})^{28.01}$. For example, the slope of i vs. $v^{1/2}$ for Fe_3O_4 -DDA-KOH is 0.0054 A/v/s, thus the electroactive area is $\sim 15.12 \times 10^{-2} \text{ cm}^2$ of the active electrode, while samples Fe_3O_4 -ABC, Fe_3O_4 -Urea and Fe_3O_4 -CNS displayed the value of $\sim 8.68 \times 10^{-2}$, 9.8×10^{-2} , and $9.81 \times 10^{-2} \text{ cm}^2$, respectively. Because of the observed lower slope values of samples in NaOH and LiOH, the effective electroactive area was lower than that observed in KOH solution. Furthermore, the linear behavior of the curves, Figure 9, for all samples, shows the presence of diffusion controlled processes. The observed non-zero intercept for Fe_3O_4 samples measured in KOH is caused by non-faradic currents contributing towards overall i_p . It is to be understood that the electrocapacitive performance of oxide nanostructured materi-

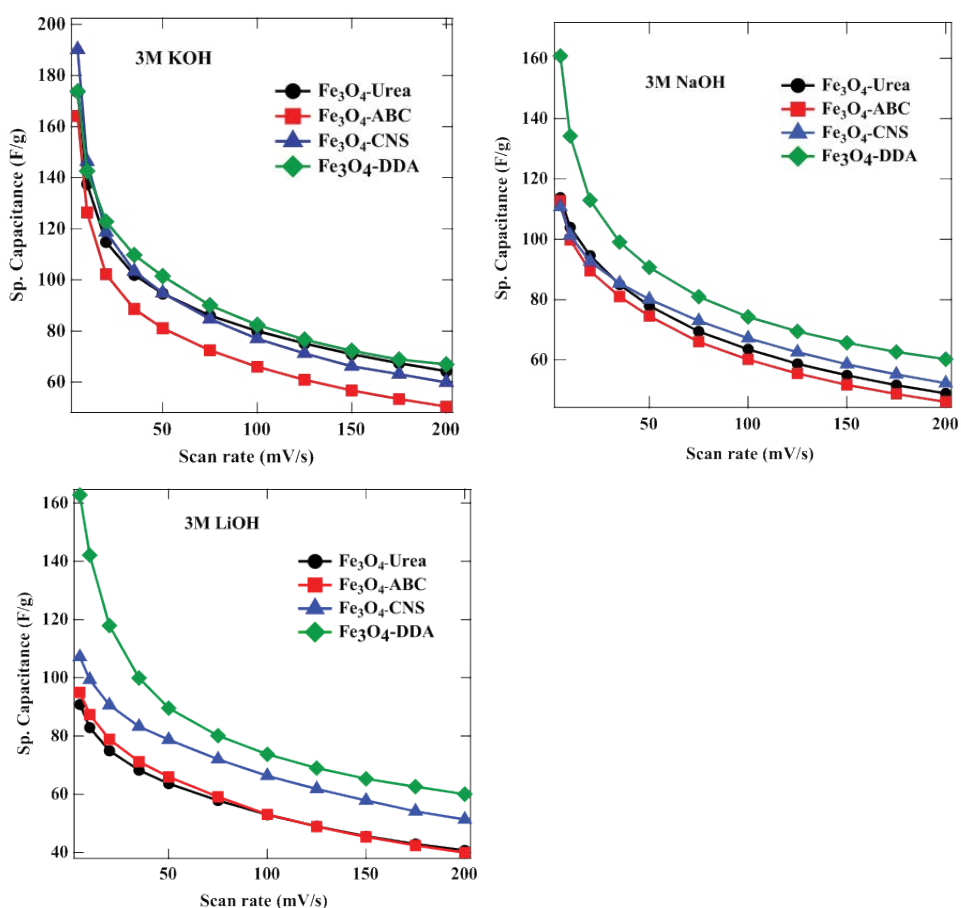


Figure 8: Comparison of specific capacitance vs. scan rate of Fe_3O_4 measured in different electrolytes.

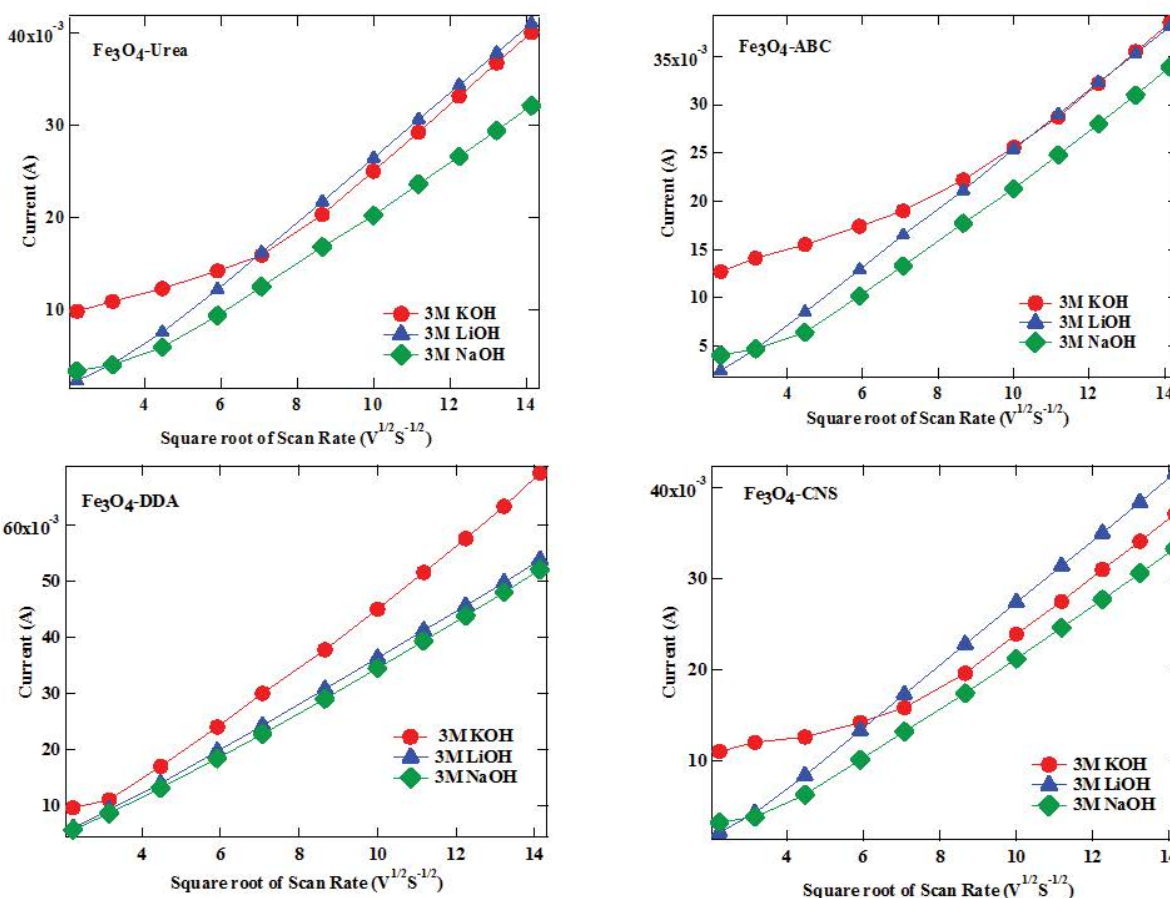


Figure 9: Comparison of peak current vs. square root of scan rate of Fe_3O_4 nanospheres measured in different electrolytes.

al complexly depends on surface area, size, crystallinity, band-gap, the number of electroactive sites, hydrophobicity, type of electrolyte used, etc [68].

Galvanostatic Charge-Discharge (GCD) measurements were performed in the voltage window of 0.0 to 0.6 V at different current densities between 0.5 A/g to 5 A/g is shown in Figure 10. The non-linearity between the potential and time indicates that the capacitance of the studied materials is not constant over the potential ranges both in charge and discharge cycle, as also confirmed by the CVs (see Figure 7). The GCD curves with a plateau show ideal pseudocapacitive property with respect to their discharging time for all electrolytes. Additional contributions to non-linear discharge curve may come from either change in equivalent series resistance and redistribution of charges within the pores of the material structure during discharging cycles [69,70]. The specific capacitance of electrodes was calculated using following equation:

$$C_{sp} = \frac{I \times t}{m \times \Delta V} \quad (11)$$

Where C_{sp} is the specific capacitance (F/g), I (A) is the charge-discharge current, ΔV (V) is the potential range, m(g) is the mass of the electroactive materials, and t(s) is

the discharging time. The dependence of C_{sp} on current density is displayed in Figure 11. Also, the C_{sp} value is listed in Table 3 measured at 1 A/g current densities. It is observed that the C_{sp} of all Fe_3O_4 electrodes decreases with increase in current density in all electrolytes. This result suggests that at high current density due to the fast charging and discharging, only part of the redox active sites of the sample contribute to C_{sp} [71]. Fe_3O_4 -DDA sample displays highest C_{sp} of ~56, 54, and 70 F/g at 1 A/g current density in KOH, NaOH and LiOH electrolyte, respectively.

The cycling performance of any electroactive material is a significant parameter to be studied for its practical applications. The cyclic performance of Fe_3O_4 -CNS and Fe_3O_4 -DDA nanospheres was carried out at 1 A/g in 3M KOH and is shown in Figure 12. Percentage retention in specific capacitance was calculated using the formula:

$$\% \text{ retention in specific capacitance} = (C\# / C1) \times 100$$

Where $C\#$ and $C1$ are specific capacitance at various cycles and at the 1st cycle, respectively. The specific capacitance of the Fe_3O_4 -CNS electrode gradually decreased at higher cycle numbers such that 39% of the initial capacitance was retained after 5,000 cycles. However, Fe_3O_4 -

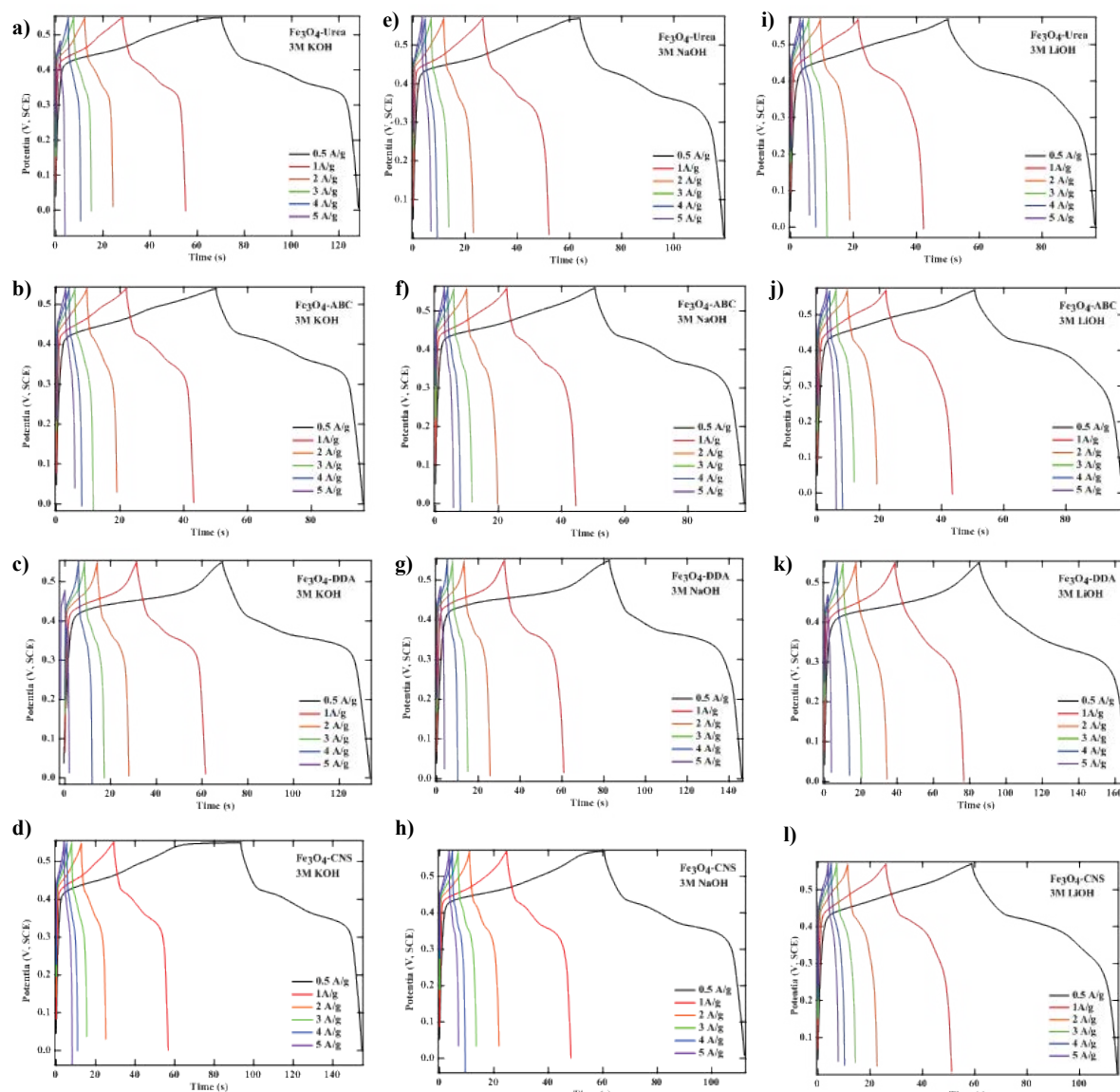


Figure 10: GCD characteristics of Fe_3O_4 nanospheres evaluated in different electrolytes.

DDA performed well and retained 107% of its full capacitance value even after 5,000 cycles. The initial increase of the specific capacitance of Fe_3O_4 -DDA can be explained by considering the gradual wetting of electrode during the GCD measurements. The fast charging and discharging leads to slow activation of the electrode materials at the initial cycles. As the cycle, the number increases the electrolyte ions gradually penetrate into the electrode materials, which activate and exposes more electroactive surface area, and thus the contribution towards specific capacitance increase. The poor cyclic performance of Fe_3O_4 -CNS can be attributed to the poor conductivity of Fe_3O_4 nanosized crystals with some degree of amorphicity. Cyclic stability test performed on Fe_3O_4 cubes prepared by hydrothermal process achieved a specific capacitance of $\sim 118 \text{ F/g}$ at 6 mA but only retained $\sim 88.7\%$ of its initial capacitance after 500 cycles [62], while Fe_3O_4

nanoparticles synthesized by a sol-gel technique delivered a specific capacitance of $\sim 185 \text{ F/g}$ at 1 mA/cm^2 [72], however, its C_{sp} deteriorated only after 200 cycles. Such poor capacitive performance and cycling stability are mainly due to the easy agglomeration of Fe_3O_4 during the charging/discharging process, which results in a low surface area and structural changes. On the other hand, Fe_3O_4 -DDA nanospheres clearly display outstanding cyclic stability even up to 5,000 cycles. Thus, Fe_3O_4 -DDA electrode meets the requirement of both long cycling performance and good rate capability, parameters that are important for the practical energy storage devices.

Figure 13 shows Ragone plots of as synthesized cobaltites [73]. The measured energy and power density for cobaltites is listed in **Table 3**. The Energy densities (E) and Power densities (P) of the electrochemical cells are calculated using the following equations [74]: $E = 1/2$

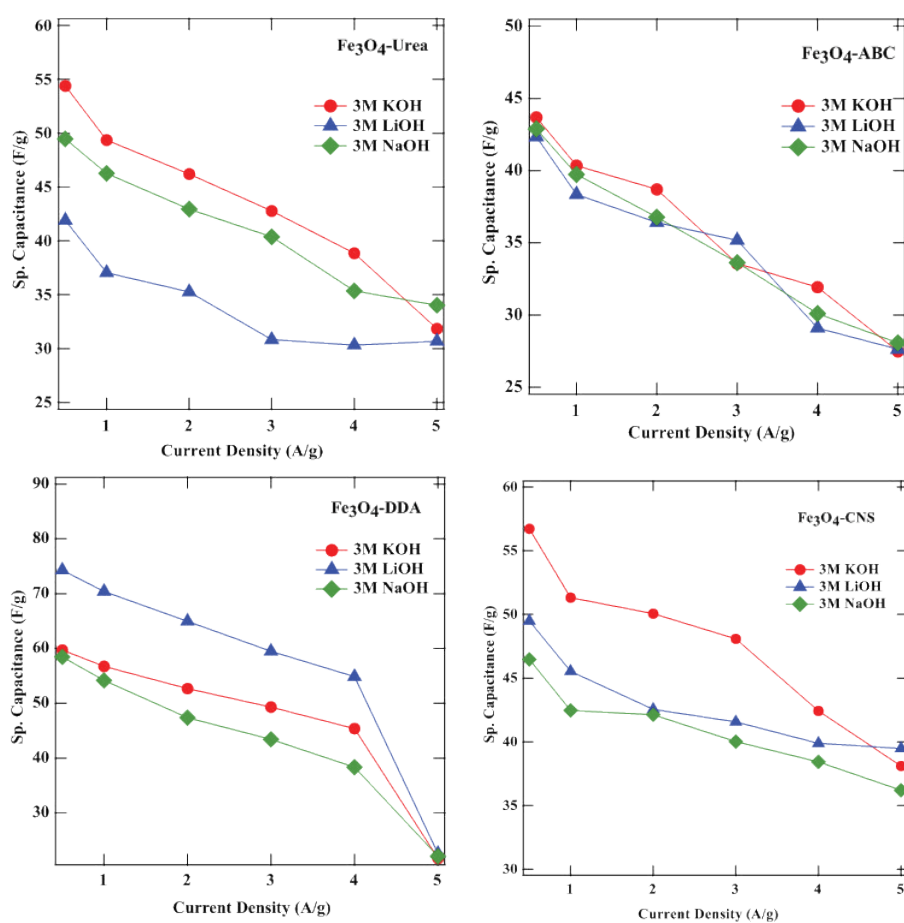


Figure 11: Comparison of specific capacitance of Fe_3O_4 nanospheres measured as a function of current density in different electrolytes.

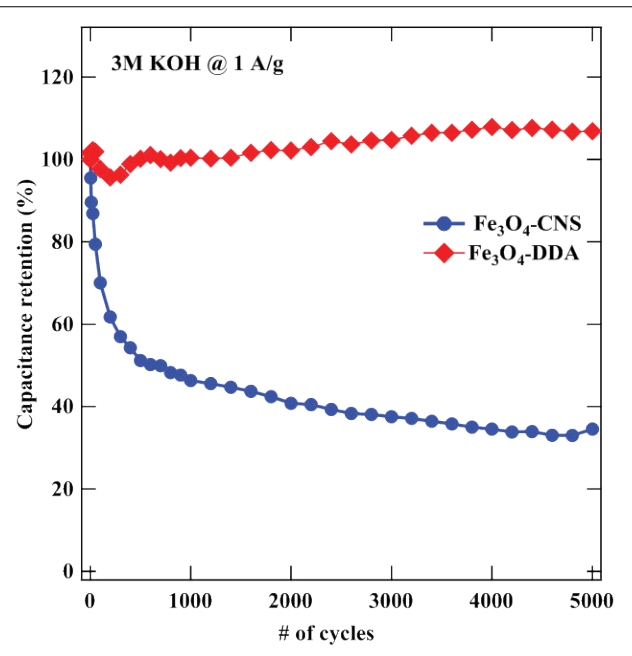


Figure 12: Comparison of cycling performance as percent capacitance retention measured for Fe_3O_4 -CNS and Fe_3O_4 -DDA in 3M KOH at 1 A/g current density.

CV^2 and $P = E/t$, where C is the specific capacitance that depends on the mass of the electrodes, V is the operating

Table 3: Specific capacitances of Fe_3O_4 nanospheres measured evaluated in different electrolytes at a fixed current density of 1 A/g.

	Specific capacitance (F/g) @ 1 A/g current density		
	KOH	NaOH	LiOH
Fe_3O_4 -urea	49.3	46.2	37.0
Fe_3O_4 -ABC	40.3	39.7	38.3
Fe_3O_4 -DDA	56.7	54.1	70.3
Fe_3O_4 -CNS	51.3	42.4	45.3

voltage of the cell and “t” is the discharge time in seconds. As known, the most important point for high-performance supercapacitors is to obtain a high energy density and meanwhile providing an outstanding power density. Although energy density performance of Fe_3O_4 hollow spheres is poor but have shown the promisingly high value of power density ~ 13000 W/kg at energy density value below 1.5 Wh/kg. Among all Fe_3O_4 electrode Fe_3O_4 -DDA, display higher energy density while Fe_3O_4 -ABC display better power density performance in all electrolytes.

The superior performance of electrodes in KOH electrolyte can be understood in terms of the molecular size of the hydrated ions. As per the literature Li^+ with ionic

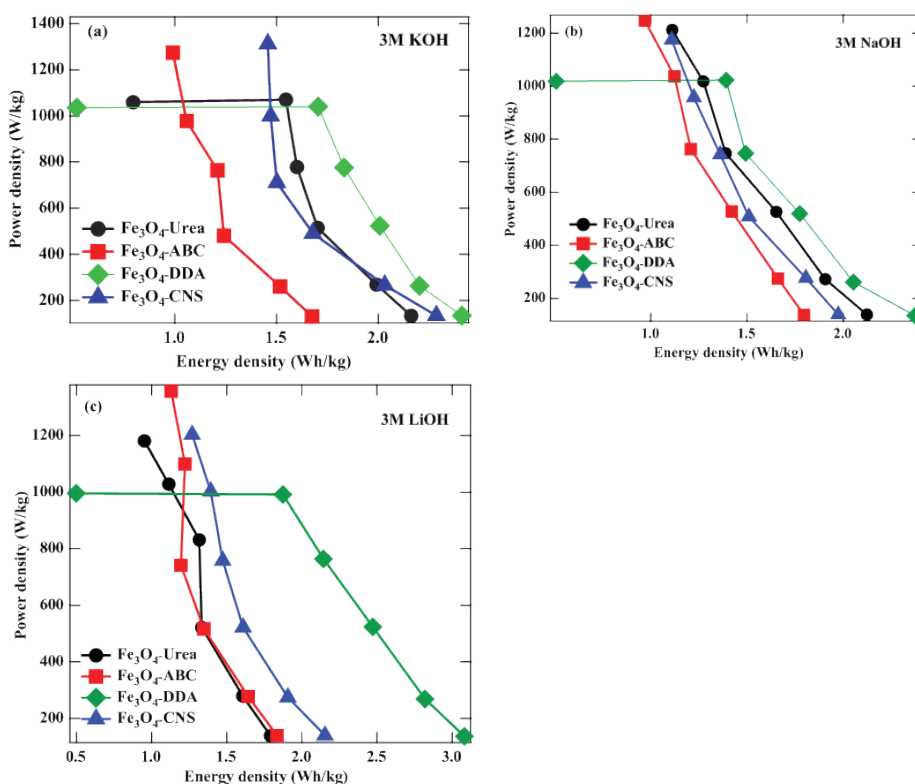


Figure 13: Power density vs. energy density, Ragone plots, of Fe_3O_4 nanospheres measured in different electrolytes.

radii 0.6 \AA is much smaller than Na^+ ionic radii of 0.95 \AA and K^+ ionic radii of 1.33 \AA [26,45]. This implies that Li^+ can easily intercalate compared to Na^+ and K^+ . However, Fe_3O_4 electrodes display highest specific capacitance in KOH followed by NaOH and LiOH, Table 2 and Table 3. This result contrary to the expectation is explained on the basis of the ionic radii of hydrated ions [75,76]. The smaller ions, in fact, form larger hydrated ions. The hydrated cation of Li^+ has ionic radii of 3.82 \AA , which is larger than the hydrated cation ionic radii of Na^+ of 3.58 \AA and hydrated cation ionic radii of K^+ of 3.31 \AA [26], which implies that Fe_3O_4 electrodes exhibit superior specific capacitance with KOH electrolyte as compared to LiOH and NaOH.

Conclusion

In summary, simple and effective surfactant and template free synthesis of magnetite hollow particles are reported. The as-synthesized Fe_3O_4 with different hydrolyzing agent show high surface area and display ferromagnetic behavior. These Fe_3O_4 hollow spheres display excellent electrocapacitive behavior with specific capacitance over 170 F/g and high rate performance. Among different hydrolyzing agents used, DDA assisted Fe_3O_4 nanospheres displayed better supercapacitor performance in all electrolytes but especially observed to have better performance in KOH. While Fe_3O_4 -ABC displayed overall poor performance in terms of electrocapacitive behavior.

Furthermore, among all electrolytes used in this study, KOH electrolyte showed comparatively better electrocapacitive performance owing to its smaller hydrated molecular size. Overall, high power density of $\sim 1300 \text{ W/kg}$ was achieved with these Fe_3O_4 electrodes. The reason for the observed superior electrocapacitive performance of Fe_3O_4 -DDA sample could be attributed to its higher crystallinity, porosity and surface area. Fe_3O_4 being low-cost material in addition to simple processing strategy offers new possibilities towards high-performance electrochemical energy storage materials.

Acknowledgement

This work was supported by the grants from FIT-DRONES at the University of Memphis, Memphis, TN. Dr. Ram K. Gupta expresses his sincere acknowledgment to the Polymer Chemistry Initiative at Pittsburg State University for providing financial and research support.

References

1. RK Gupta, J Candler, S Palchoudhury, K Ramasamy, BK Gupta (2016) Flexible and high performance supercapacitors based on $\text{nico}_{2}\text{o}_4$ for wide temperature range applications. *Scientific Reports* 5.
2. BE Conway, V Birss, J Wojtowicz (1997) The role and utilization of pseudocapacitance for energy storage by supercapacitors. *J Power Sour* 66: 1-14.
3. E Mitchell, RK Gupta, BK Gupta, PK Kahol, M Shahabuddin, et al. (2015) Ultrathin porous hierarchically textured

- NiCo₂O₄-graphene oxide flexible nanosheets for high-performance supercapacitors. *New J Chem* 39: 2181-2187.
4. ML Huang, CD Gu, X Ge, XL Wang, JP Tu (2014) NiO nanoflakes grown on porous graphene frameworks as advanced electrochemical pseudocapacitor materials. *J Power Sour* 259: 98-105.
 5. X Yu, B Lu, Z Xu (2014) Super long-life supercapacitors based on the construction of nanohoneycomb-Like strongly coupled comoo₄-3D graphene hybrid electrodes. *Adv Mater* 26: 1044-1051.
 6. P Yang, Y Ding, Z Lin, Z Chen, Y Li, et al. (2014) Low-cost high-performance solid-state asymmetric supercapacitors based on MnO₂ nanowires and Fe₂O₃ nanotubes. *Nano Lett* 14: 731-736.
 7. KK Lee, S Deng, HM Fan, S Mhaisalkar, HR Tan, et al. (2012) α-Fe₂O₃ nanotubes-reduced graphene oxide composites as synergistic electrochemical capacitor materials. *Nanoscale* 9: 2958-2961.
 8. H Adhikari, D Neupane, CK Ranaweera, J Candler, RK Gupta, et al. (2017) Template-free synthesis of hierarchical mixed-metal cobaltites: Electrocapacitive and theoretical study. *Electrochimica Acta* 225: 514-524.
 9. SB Yang, XL Feng, S Ivanovici, K Mullen (2010) Fabrication of graphene-encapsulated oxide nanoparticles: towards high-performance anode materials for lithium storage. *Angew Chem Int Ed* 49: 8408-8411.
 10. ZC Xu, YL Hou, SH Sun (2007) Magnetic core/shell Fe₃O₄/Au and Fe₃O₄/Au/Ag nanoparticles with tunable plasmonic properties. *J Am Chem Soc* 129: 8698-8699.
 11. K Cheng, S Peng, CJ Xu, SH Sun (2009) Porous hollow Fe₃O₄ nanoparticles for targeted delivery and controlled release of cisplatin. *J Am Chem Soc* 131: 10637-10644.
 12. NL Wu (2002) Nanocrystalline oxide supercapacitors. *Materials Chem Phys* 75: 6-11.
 13. MY Ho, PS Khiew, D Isa, TK Tan, WS Chiu, et al. (2014) Nano Fe₃O₄-activated carbon composites for aqueous supercapacitors. *Sains Malaysiana* 43: 885-894.
 14. T Brousse, D Belanger (2003) A Hybrid Fe₃O₄-MnO₂ capacitor in mild aqueous electrolyte. *Electrochim Solid-State Lett* 6: 244-248.
 15. SY Wang, KC Ho, SL Kuo, NL Wu (2006) Investigation on capacitance mechanisms of Fe₃O₄ electrochemical capacitors. *J Electrochemical Soc* 153: 75-80.
 16. GA Tiruye, DM Torrero, J Palma, M Anderson, R Marcilla (2015) All-solid state supercapacitors operating at 3.5 V by using ionic liquid based polymer electrolytes. *J Power Sources* 279: 472-480.
 17. F Gao, G Shao, J Qu, S Lv, Y Li, et al. (2015) Tailoring of porous and nitrogen-rich carbons derived from hydrochar for high-performance supercapacitor electrodes. *Electrochim Acta* 155: 201-208.
 18. M Selvam, SR Srither, K Saminathan, V Rajendran (2015) Chemically and electrochemically prepared graphene/MnO₂ nanocomposite electrodes for zinc primary cells: a comparative study. *Ionics* 21: 791-799.
 19. Y Tang, Y Liu, S Yu, F Gao, Y Zhao (2015) Comparative study on three commercial carbons for supercapacitor applications. *Russ J Electrochem* 51: 77-85.
 20. KV Sankar, RK Selvan (2015) Improved electrochemical performances of reduced graphene oxide based supercapacitor using redox additive electrolyte. *Carbon* 90: 260-273.
 21. V Sahu, S Shekhar, RK Sharma, G Singh (2015) Ultrahigh performance supercapacitor from lacy reduced graphene oxide nanoribbons. *ACS Appl Mater Interfaces* 7: 3110-3116.
 22. NL Wu, YP Lan, CY Han, SY Wang, LR Shiue (2002) Electrochemical capacitor and hybrid power sources. In: RJ Brodd, DH Doughty, JH Kim, M Morita, K Naoi, et al. *The electrochemical society proceedings series*. Pennington, NJ, 95.
 23. NL Wu, SY Wang, CY Han, DS Wu, LR Shiue (2003) Electrochemical capacitor of magnetite in aqueous electrolytes. *J Power Sources* 113: 173-178.
 24. SY Wang, NL Wu (2003) Operating characteristics of aqueous magnetite electrochemical capacitors. *J Appl Electrochem* 33: 345-348.
 25. LR Shiue, NL Wu, DS Wu, CW Chao, YP Lan (2004) Electrochemical capacitor with electrode material for energy storage.
 26. R Wang, Q Li, L Cheng, H Li, B Wang, et al. (2014) Electrochemical properties of manganese ferrite-based supercapacitors in aqueous electrolyte: The effect of ionic radius. *Colloid Surfaces A Phys Eng Aspects* 457: 94-99.
 27. Y Liu, Y Wang, S Zhou, S Lou, L Yuan, et al. (2012) Electrochemical properties of manganese ferrite-based supercapacitors in aqueous electrolyte: The effect of ionic radius. *Appl Mater Interfaces* 4: 4913.
 28. MM Goswami, C Dey, A Bandyopadhyay, D Sarkar, M Ahir (2016) Micelles driven magnetite (Fe₃O₄) hollow spheres and a study on AC magnetic properties for hyperthermia application. *J Magn Magn Mater* 417: 376-381.
 29. Y Cong, G Wang, M Xiong, Y Huang, Z Hong, et al. (2008) A Facile interfacial reaction route to prepare magnetic hollow spheres with tunable shell thickness. *Langmuir* 24: 6624-6629.
 30. P Hu, L Yu, A Zuo, C Guo, F Yuan (2009) Fabrication of monodisperse magnetite hollow spheres. *J Phys Chem C* 113: 900-906.
 31. X Lin, G Ji, Y Liu, Q Huang, Z Yang, et al. (2012) Formation mechanism and magnetic properties of hollow Fe₃O₄ nanospheres synthesized without any surfactant. *Cryst Eng Comm* 14: 8658-8663.
 32. Wilson, SR Mishra, R Gupta, K Ghosh (2012) Preparation and photocatalytic properties of hybrid core-shell reusable CoFe₂O₄-ZnO nanospheres. *J Magn Magn Mater* 324: 2597-2601.
 33. G Vaidyanathan, S Sendhilnathan, R Arulmurugan (2007) Structural and magnetic properties of Co_{1-x}Zn_xFe₂O₄ nanoparticles by co-precipitation method. *J Magn Magn Mater* 313: 293-299.
 34. DH Han, JP Wang, HL Lou (1994) Crystallite size effect on saturation magnetization of fine ferrimagnetic particles. *J Magn Magn Mater* 136: 176-182.
 35. C Dong (1999) PowderX: Windows-95-based program for

- powder X-ray diffraction data processing. *J Appl Cryst* 32: 838-839.
36. MZC Hu, MT Harris, CH Byers (1998) Nucleation and growth for synthesis of nanometric zirconia particles by forced hydrolysis. *J Coll Inter Sci* 198: 87-99.
37. K Kakiuchi, E Hosono, T Kimura, H Imai, S Fujihara (2006) Fabrication of mesoporous ZnO nanosheets from precursor templates grown in aqueous solutions. *J Sol-Gel Sci Technol* 39: 63-72.
38. JZ Marinho, FC Romeiro, SCS Lemos, FV Motta, CS Riccardi, et al. (2012) Urea-Based synthesis of Zinc oxide nanostructures at low temperature. *J Nanomater* 2012: 427172.
39. SE Skrabalak, BJ Wiley, M Kim, EV Formo, YN Xia (2008) On the polyol synthesis of silver nanostructures: glycolaldehyde as a reducing agent. *Nano Lett* 8: 2077-2081.
40. WB Smith (2002) Ethylene glycol to acetaldehyde-dehydration or a concerted mechanism. *Tetrahedron* 58: 2091-2094.
41. Z Kozakova, I Kuritka, NE Kazantseva, V Babayan, M Pastorek, et al. (2015) The formation mechanism of iron oxide nanoparticles within the microwave-assisted solvothermal synthesis and its correlation with the structural and magnetic properties. *Dalton Trans* 44: 21099-21108.
42. S Frantisek, M Marek, PM Adler (1999) Modeling capillary condensation hysteresis cycles in reconstructed porous media. *AIChE Journal* 45: 1901-1912.
43. LP Zhu, HM Xiao, WD Zhang, G Yang, SY Fu (2008) One-pot template-free synthesis of monodisperse and single-crystal magnetite hollow spheres by a simple solvothermal route. *Cryst Growth Des* 3: 957-963.
44. C Largeot, C Portet, J Chmiola, P Taberna, Y Gogotsi, et al. (2008) Relation between the ion size and pore size for an electric double-layer capacitor. *J Am Chem Soc* 130: 2730-2731.
45. S Kuyucak, OS Andersen, Shin Ho Chung (2001) Models of permeation in ion channels. *Rep Prog Phys* 64: 1427.
46. J Zhi, Y Wang, S Deng, A Hu (2014) Study on the relation between pore size and supercapacitance in mesoporous carbon electrodes with silica-supported carbon nanomembranes. *RSC Adv* 76: 40296-40300.
47. S Kondrat, CR Perez, V Presser, Y Gogotsi, AA Kornyshev (2012) Effect of pore size and its dispersity on the energy storage in nanoporous supercapacitors. *Energy Environ Sci* 5: 6474-6479.
48. D Yu, X Sun, J Zou, Z Wang, F Wang, et al. (2006) Oriented assembly of Fe_3O_4 nanoparticles into monodisperse hollow single-crystal microspheres. *J Phys Chem B* 110: 21667-21671.
49. CZ Wu, Y Xie, LY Lei, SQ Hu, CZ OuYang (2006) Synthesis of new-phased VOOH hollow "Dandelions" and their application in lithium-ion batteries. *Adv Mater* 18: 1727-1732.
50. H Wang, W Geng, Y Wang (2011) Preparation of nanoparticles and hollow spheres of $\alpha\text{-Fe}_2\text{O}_3$ and their properties. *Res Chem Intermed* 37: 389-395.
51. DE Zhang, XJ Zhang, XM Ni, JM Song, HG Zheng (2007) Fabrication and characterization of Fe_3O_4 octahedrons via an EDTA-assisted route. *Cryst Growth Des* 7: 2117-2119.
52. Q Song, ZJ Zhang (2004) Shape control and associated magnetic properties of spinel cobalt ferrite nanocrystals. *J Am Chem Soc* 126: 6164-6168.
53. CR Vestal, ZJ Zhang (2003) Effects of surface coordination chemistry on the magnetic properties of MnFe_2O_4 spinel ferrite nanoparticles. *J Am Chem Soc* 125: 9828-9833.
54. LP Zhu, HM Xiao, SY Fu (2007) Template-free synthesis of monodispersed and single-crystalline cantaloupe-like Fe_2O_3 superstructures. *Cryst Growth Des* 7: 177-182.
55. Lee Blaney (2017) Magnetite (Fe_3O_4): Properties, synthesis, and applications. Leighie preserve, Leighie University 15.
56. L O'Neill, C Johnston, PS Grant (2015) Enhancing the supercapacitor behaviour of novel $\text{Fe}_3\text{O}_4/\text{FeOOH}$ nanowire hybrid electrodes in aqueous electrolytes. *J Power Sources* 274: 907-915.
57. I Oh, M Kim, J Kim (2015) Fe_3O_4 /carbon coated silicon ternary hybrid composite as supercapacitor electrodes. *J Appl Surf Sci* 328: 222-228.
58. JW Lee, AS Hall, JD Kim, TE Mallouk (2012) A facile and template-free hydrothermal synthesis of Mn₃O₄ nanorods on graphene sheets for supercapacitor electrodes with Long Cycle stability. *Chem Mater* 24: 1158-1164.
59. D Ghosh, S Giri, CK Das (2014) Hydrothermal synthesis of platelet $\beta\text{Co(OH)}_2$ and Co_3O_4 : Smart electrode material for energy storage application. *Environ Prog Sustain Energy* 33: 1059-1064.
60. H Yi, H Wang, Y Jing, T Peng, X Wang (2015) Asymmetric supercapacitors based on carbon nanotubes@NiO ultra-thin nanosheets core-shell composites and MOF-derived porous carbon polyhedrons with super-long cycle life. *J Power Sources* 285: 281-290.
61. E Mitchell, RK Gupta, K Mensah-Darkwa, D Kumar, K Ramasamy, et al. (2014) Facile synthesis and morphogenesis of superparamagnetic iron oxide nanoparticles for high-performance supercapacitor applications. *New J Chem* 38: 4344-4350.
62. J Chen, K Huang, S Liu (2009) Hydrothermal preparation of octadecahedron Fe_3O_4 thin film for use in an electrochemical supercapacitor. *Electrochim Acta* 55: 1-5.
63. D Guan, Z Gao, W Yang, J Wang, Y Yuan, et al. (2013) Hydrothermal synthesis of carbon nanotube/cubic Fe_3O_4 nanocomposite for enhanced performance supercapacitor electrode material. *J Mater Sci Eng B* 178: 736-743.
64. JEB Randles (1948) A cathode ray polarograph. Part II.-The current-voltage curves. *Trans Faraday Soc* 44: 327-338.
65. Sevcik (1948) Oscillographic polarography with periodical triangular voltage. *Collect Czech Chem Commun* 13: 349-377.
66. C Hu, J Deng, X Xiao, X Zhan, K Huang, et al. (2015) Determination of dimetridazole using carbon paste electrode modified with aluminum doped surface molecularly imprinted siloxane. *Electrochimica Acta* 158: 298-305.
67. E Samson, J Marchand, KA Snyder (2003) Calculation of ionic diffusion coefficients on the basis of migration test results. *Materials and Structures/Materiaux et Constructions* 36: 156-165.
68. VD Nithya, N Sabari Arul (2016) Progress and development of Fe_3O_4 electrodes for supercapacitors. *J Mater Chem A* 4: 10767-10778.

69. S Chen, J Zhu, X Wu, Q Han, X Wang (2010) Graphene Oxide-MnO₂ nanocomposites for supercapacitors. *ACS Nano* 4: 2822-2830.
70. J Chen, N Xia, T Zhou, S Tan, F Jiang, et al. (2009) Mesoporous carbon spheres: Synthesis, Characterization and Supercapacitance. *Int J Electrochem Sci* 4: 1063-1073.
71. JG Wang, Y Yang, ZH Huang, F Kang (2012) Interfacial synthesis of mesoporous MnO₂/polyaniline hollow spheres and their application in electrochemical capacitors. *J Power Sources* 204: 236-243.
72. J Mu, B Chen, Z Guo, M Zhang, Z Zhang, et al. (2011) Highly dispersed Fe₃O₄ nanosheets on one-dimensional carbon nanofibers: Synthesis, formation mechanism, and electrochemical performance as supercapacitor electrode materials. *Nanoscale* 3: 5034-5040.
73. BD McCloskey (2015) Expanding the ragone plot: Pushing the limits of energy storage. *J Phys Chem Lett* 6: 3592-3593.
74. J Candler, T Elmore, BK Gupta, L Dong, S Palchoudhury, et al. (2015) New insight into high-temperature driven morphology reliant CoMoO₄ flexible supercapacitors. *New J Chem* 39: 6108-6116.
75. MM Vadiyar, SC Bhise, SK Patil, SS Kolekar, JY Chang, et al. (2016) Comparative study of individual and mixed aqueous electrolytes with ZnFe₂O₄ nano-flakes thin film as an electrode for supercapacitor application. *Chemistry Select* 1: 959-966.
76. Z Chang, Y Yang, M Li, X Wang, Y Wu (2014) Green energy storage chemistries based on neutral aqueous electrolytes. *J Mater Chem A* 2: 10739-10755.